Journal of Power Sources 187 (2009) 136–147

Contents lists available at ScienceDirect

Journal of Power Sources

journal homepage: www.elsevier.com/locate/jpowsour

An inverse geometry design problem in optimizing the shape of the gas channel for a proton exchange membrane fuel cell

Cheng-Hung Huang[a,*], Liang-Yu Chen[a], Sin Kim[b]

[a] Department of Systems and Naval Mechantronic Engineering, National Cheng Kung University, Tainan, Taiwan, ROC
[b] Department of Nuclear and Energy Engineering, Cheju National University, Cheju 690-756, Republic of Korea

ARTICLE INFO

Article history:
Received 3 September 2008
Received in revised form 17 October 2008
Accepted 17 October 2008
Available online 6 November 2008

Keywords:
Proton exchange membrane fuel cell
Gas channel design
Inverse design problem

ABSTRACT

The inverse design problem technique presented in this paper is intended for optimizing the shape of the gas channel at the cathode side in a proton exchange membrane fuel cell (PEMFC). The technique uses the desired current densities located on a carbon plate near the outlet of the channel at the cathode side as a starting point. The desired current density distributions can be obtained by modifying the current density distributions of the existing PEMFC with rectangular gas channels. The geometry of the redesigned gas channel is generated using a B-spline curve method, which enables the shape of the fuel channel to be completely specified using only a small number of control points, thus applying the technique of parameter estimation for the inverse design problem. Results show that by utilizing the redesigned optimal gas channel, the total current of the PEMFC can be increased, and at the same time the phenomenon of saturated water accumulation in the channel can be greatly reduced.

1. Introduction

In order to adapt to environmental change as well as the world's current energy crisis, in the past several years researchers around the world have been focusing on developing renewable resources including geothermal energy, solar energy, wind energy, tidal energy and hydrogen energy to substitute for conventional resources such as coal, oil, and natural gas. Fuel cells have several advantages over conventional power generation appliances, and can thus be considered major power-generating devices in the future. In a fuel cell, chemical energy is converted to electrical energy directly, with little heat production. This implies that the efficiency of a fuel cell is not limited by the Carnot cycle efficiency.

In general, fuel cells produce less toxic by-products than conventional appliances, thus making them environment-friendly. Moreover, fuel cells are very quiet during operation and can be of various sizes; these features will make them ideal for installation in any place. The application range of fuel cells is very wide, from a soldier's equipment on the battlefield to huge power generators for residential and industrial applications. Most fuel cells operate at low temperatures (around 70 °C), with the exception of solid oxide fuel cells, and this, added to the fact that they do not have any moving parts, will make them easy to design from a materials standpoint.

Significant progress in the development of fuel cell technology has been achieved by an increasing number of experimental and theoretical studies [1–6]. One of the most promising types of fuel cells, the proton exchange membrane fuel cell (PEMFC), is currently being aggressively researched due to its significant advantages in portable electronic applications over conventional battery systems. It also meets more stringent emissions standards, because far fewer pollutants are produced by it than by internal combustion engines. Common flow-field designs for this fuel cell include the conventional flow fields, i.e., parallel flow field, Z-type flow field, and serpentine flow field. Due to the fact that flow-field design in the fuel cell is important in determining the fuel cell's performance, many researchers have examined this issue in recent years. However, for simplicity, in the present study only the case of the parallel flow field is examined.

In the PEMFC, the maximum current densities will appear at the flow channel inlets and decrease along the channels to the outlets. This is due to the fact that the oxygen is gradually consumed and liquid water is accumulated due to the electrochemical reaction along the flow channels. For this reason, if the large amount of liquid water accumulation can be removed efficiently, the current densities along the channels will be increased and the performance of the PEMFC must therefore be improved significantly. Many efforts have been devoted to optimizing the flow field design in order to improve the cell performance [7–12]. This can also be done by redesigning the shape of the gas channel, applying the technique of the inverse design problem [13–15].

* Corresponding author. Tel.: +886 6 274 7018; fax: +886 6 274 7019.
E-mail address: chhuang@mail.ncku.edu.tw (C.-H. Huang).

0378-7753/$ – see front matter © 2008 Elsevier B.V. All rights reserved.
doi:10.1016/j.jpowsour.2008.10.093

The direct PEMFC problems are concerned with the determination of the current densities, saturated water and pressure drops in the cell when the operational conditions, system parameters and the shape of gas channels are all specified. In contrast, the inverse geometry design problem for the PEMFC considered in this paper involves the determination of the optimal shape of gas channels based on the requirement of desired current density on the upper carbon plate of the redesigned gas channel at the cathode.

Recently, Cheng et al. [16] applied the simplified conjugate gradient method (SCGM) in the PEMFC for the optimization of the geometric parameters of the fuel cells and obtained good estimations. Yan et al. [17] proposed a parallel flow channel design with tapered heights or widths to improve reactant utilization efficiency for PEMFCs. In their study, the tapered channel designs are used and the flow area contraction along the flow channel leads to increased reactant velocities, thereby enhancing the reactant transport through the porous layers, reactant utilization and liquid water removal. However, one should note that these tapered channels are designed manually and are not based on the algorithm of the inverse design problem.

With this in mind, the technique of the inverse design problem should be used to design the optimal gas channel geometry in accordance with the desired current density distributions of the cell. The desired current density distributions can be obtained by modifying the existing current density distributions in the PEMFC. A B-spline curve is utilized to simulate the shape of the gas channel, and therefore the shape parameters in this formulation are the coordinates of each control point, i.e., this limited number of control points becomes the set of parameters controlling the gas channel geometry. In the present study, the task is to redesign the gas channel geometry for parallel flow arrangement, based on both the original gas channel geometry and the new desired current density distributions. The originality of this study lies in that the present algorithm can design the optimal shape of gas channel that satisfies the desired current density.

For the present geometry design problem, due to its inherent nature, a complete regeneration of the mesh is required as the geometry evolves. Moreover, the continuous evolution of the geometry itself poses certain difficulties in arriving at analytical or numerical solutions. For this reason, it is necessary to use an efficient technique that can handle a problem with irregular surface geometry, especially in this 3D application.

This paper addresses the development of an efficient method for parameter estimation, i.e., the Levenberg–Marquardt algorithm, in estimating the optimal gas channel geometry that satisfies the desired current density distributions. The Levenberg–Marquardt method has proven to be a powerful algorithm in inverse design calculations. This inverse design method had been applied to predict the form of a ship's hull in accordance with the desired hull pressure distribution by Huang et al. [13]. Subsequently, Chen and Huang [14] applied it to predict an unknown hull form based on the preferable wake distribution in the propeller disk plane. Chen et al. [15] further applied it to the aspect of optimal design for a bulbous bow.

In Section 2 of this paper, the algorithm used to calculate the cell current density distribution, i.e., the direct problem, is explained. The method of B-spline curves is described in Section 3. The inverse design problem, involving the definition of a cost function and the Levenberg–Marquardt algorithm, is addressed in Section 4. Finally, a computational procedure is summarized in Section 5.

2. The direct problem

Fuel cells constitute an important alternative to power generation by engines or turbines. With an increasing trend towards reduced emissions and higher efficiency, fuel cells are emerging rapidly as the technology of choice for power generation in the new century.

The PEMFC consists of an anode flow channel, an anode diffuser layer, an anode catalyst layer, a proton exchange membrane, a cathode catalyst layer, a cathode diffuser layer, and a cathode flow channel. To simplify the analysis, it is assumed that the gas mixtures are ideal gases; the flow field is steady, laminar and incompressible; the cell is isothermal; the electrochemical reaction only takes place in the catalyst layer; and the cell structures in the diffuser layers, the catalyst layers, and the proton exchange membrane are made of isotropic and homogeneous porous material.

The gas channels and the gas diffusion layers inside the fuel cells are designed to allow the reactant gases to diffuse uniformly into the catalyst layers, and at the same time, to prevent excessive increase in electrical resistance against the released electrons from the catalyst layers. The porous layers include the gas diffusion layers and the catalyst layers, in which the mass, momentum, and species equations for the flows should be derived based on the non-Darcy law.

The mathematical models for the present 3D PEMFC involving four groups of differential equations, namely, (a) mass, momentum, and species transport phenomena in the gas channels (GC) and the porous layers—i.e., gas diffusion layer (GDL) and catalyst layer (CL); (b) electrochemical reactions in the catalyst layers; (c) ionic conduction taking place in the catalyst layers and the proton exchange membrane; (d) electronic conduction in the porous layers and the carbon plates (CP). These governing equations are described below [16,17].

2.1. Mass, momentum, and species transport equations

The conservation equations for mass, momentum, and species can be used to model the gas flows in the gas channels, gas diffusion layer and catalyst layer for the PEMFC. These equations are given below for mass, momentum and species equations, respectively:

$$\nabla \cdot (\varepsilon \rho \vec{U}) = 0, \tag{1}$$

$$\nabla \cdot (\varepsilon \rho \vec{U}\vec{U}) = -\varepsilon \nabla P + \nabla \cdot (\varepsilon \tau) + \frac{\varepsilon^2 \mu \vec{U}}{k}, \tag{2}$$

$$\nabla \cdot (\varepsilon \rho U Z_n) = \nabla \cdot (D_n^{\text{eff}} \nabla Z_n) + S_n. \tag{3}$$

Here $\vec{U}$ denotes the gas velocity vector, ε and k are the porosity and permeability of the porous layers, respectively, and τ is the fluid stress tensor. The fuel gases at the anode side and cathode side are H_2 and O_2, respectively. Z_n represents the species mass fraction of species n. It should be noted that $\varepsilon = 1$ and $k = \infty$ imply pure fluid flows in the gas channels.

The effective mass diffusivity D_n^{eff} of species n can be obtained by using Bruggemann's equation, and is calculated as

$$D_n^{\text{eff}} = \varepsilon^{\theta} D_n, \tag{4}$$

where θ is the Bruggemann coefficient of the porous layer and D_n is the mass diffusivity of species n. In Eq. (3), S_n represents the source term of species n, which is due to the electrochemical reactions in the catalyst layers.

2.2. Electrochemical reaction equations

During the reaction, H_2 and O_2 are consumed in the catalyst layers of the anode and cathode, respectively, and H_2O is the product of the reaction at the cathode. The source terms for different species

are defined as follows:

$$S_{H_2} = \frac{-I_a}{2F}, \tag{5}$$

$$S_{O_2} = \frac{I_c}{4F}, \tag{6}$$

$$S_{H_2O} = \frac{-I_c}{2F}, \tag{7}$$

where F is the Faraday constant, while I_a and I_c are the transfer current densities at the anode and the cathode, respectively. These values can be obtained based on the Butler–Volmer condition:

$$I_a = I_{a,ref}\left(\frac{Z_{H_2}}{Z_{H_2,ref}}\right)^{r_a}\left[\exp\left(\frac{\alpha_{a,a}F\eta}{RT}\right) - \exp\left(\frac{-\alpha_{a,c}F\eta}{RT}\right)\right], \tag{8}$$

$$I_c = I_{c,ref}\left(\frac{Z_{O_2}}{Z_{O_2,ref}}\right)^{r_c}\left[\exp\left(\frac{\alpha_{c,a}F\eta}{RT}\right) - \exp\left(\frac{-\alpha_{c,c}F\eta}{RT}\right)\right], \tag{9}$$

where $I_{a,ref}$ and $I_{c,ref}$ are the reference transfer current densities, and r_a and r_c the concentration parameters at the anode and the cathode, respectively. The terms $\alpha_{a,a}$ and $\alpha_{a,c}$ are the anodic and the cathodic charge transfer coefficients for the anode reaction, while $\alpha_{c,a}$ and $\alpha_{c,c}$ are the anodic and the cathodic charge transfer coefficients for the cathode reaction. $Z_{H_2,ref}$ and $Z_{O_2,ref}$ are the reference concentrations at which the exchange current densities are obtained.

2.3. Ionic conduction equations

The ionic conduction occurs in the catalyst layers and the proton exchange membrane, since protons of hydrogen (H+) are generated in the anode catalyst layer and then move through the proton exchange membrane toward the cathode catalyst layer to react with oxygen and the returning electrons. The ionic conduction equation for determining the phase potential, φ, in the catalyst layers is obtained as

$$-\nabla\cdot(\Gamma_{CL}^{eff}\nabla\varphi_{CL}) = \xi_{CL}, \tag{10}$$

where φ_{CL} and Γ_{CL}^{eff} are the phase potential and effective ionic conductivity of the catalyst layers, respectively. The effective ionic conductivity, Γ_{CL}^{eff}, is evaluated by using the following equation:

$$\Gamma_{CL}^{eff} = \varepsilon_{s,CL}^{\theta_{CL}} \times \Gamma_{s,CL}. \tag{11}$$

The effective ionic conductivity of the catalyst layer, Γ_{CL}^{eff}, increases with the porosity of solid catalyst particles in the catalyst layer, $\varepsilon_{s,CL}$. The ionic conduction equation for the membrane can be expressed as

$$\nabla\cdot(\Gamma_m\nabla\varphi_m) = 0, \tag{12}$$

where Γ_m is the ionic conductivity and φ_m is the phase potential of the membrane. Springer et al. [18] suggested that the expression for ionic conductivity of the membrane can be expressed as

$$\Gamma_m(T) = \Gamma_{m,ref}\times\exp\left[1268\times\left(\frac{1}{303}-\frac{1}{T}\right)\right], \tag{13}$$

where the reference ionic conductivity $\Gamma_{m,ref}$ is given as

$$\Gamma_{m,ref} = 0.005239\lambda - 0.00326. \tag{14}$$

Based on the experimental data, the water content of the membrane, λ, depends on the dimensionless water activity in the membrane, 'a', which is defined as the gas partial pressure of water at equilibrium with the membrane divided by the saturation pressure of water vapor at the operating temperature. The expression of water activity in the membrane can be obtained as

$$a = \frac{X_{H_2O}P}{P_{sat}}. \tag{15}$$

The saturation pressure of water vapor, P_{sat}, can be computed by

$$P_{sat} = 10^{-2.1794+0.02953(T-273.15)-9.1837(T-273.15)^2\times10^{-5}+1.4454(T-273.15)^3\times10^{-7}} \tag{16}$$

with T in K.

The relationship between λ and a can be obtained as

$$\lambda = \begin{cases} 0.043 + 17.81a - 39.85a^2 + 36.0a^3; & 0 \le a \le 1 \\ 14.0 + 1.4(a-1); & 1 < a \le 3 \\ 16.8; & 3 < a \end{cases}. \tag{17}$$

Finally, based on the solution for the phase potential φ, the distribution of local ionic current density, $\bar{I}$, may be further determined by the following expression:

$$\bar{I} = -\Gamma\nabla\varphi. \tag{18}$$

2.4. Electronic conduction equations

The carbon plate, the GDL, and the catalyst layers all serve as conductors for electric current. In the carbon plate and the GDL, there is no electrochemical reaction taking place. The electrochemical reactions only take place in the catalyst layers. Due to the electrochemical reactions activated in the catalyst layers, there exists a source term in the electronic conduction equation. Therefore, the electronic conduction equation for these three components can be expressed in the following general form:

$$\nabla\cdot(\sigma_d^{eff}\nabla\phi) = \xi_d. \tag{19}$$

Here, 'd' represents three different layers, i.e., the carbon plate, the GDL, and the catalyst layer, respectively. The term ϕ denotes the electronic potential and σ_d^{eff} is the effective electronic conductivity. The effective electronic conductivity for the carbon plate (CP) can be taken as a constant, while the effective electronic conductivities for the porous gas diffusion layer and the catalyst layer can be determined in terms of the porosity based on Bruggemann's equation. The equations are listed below:

$$\sigma_{CP}^{eff} = \sigma_{CP}, \tag{20}$$

$$\sigma_{GDL}^{eff} = (1-\varepsilon_{GDL})^{\theta_{GDL}}\times\sigma_{GDL}, \tag{21}$$

$$\sigma_{CL}^{eff} = \varepsilon_{s,CL}^{\theta_{CL}}\times\sigma_{s,CL}. \tag{22}$$

Here, $\varepsilon_{s,CL}$ and $\sigma_{s,CL}$ denote the volume fraction (porosity) and electronic conductivity, respectively, of solid catalyst particles in the catalyst layer. In addition, the source term ξ_d in Eq. (10) for the carbon plate, porous gas diffusion layer and catalyst layer can be expressed as

$$\xi_{CP} = 0, \tag{23}$$

$$\xi_{GDL} = 0, \tag{24}$$

$$\xi_{CL} = \begin{cases} \xi_{CL,a} = -I_a \\ \xi_{CL,c} = I_c \end{cases}. \tag{25}$$

Boundary conditions at the anode flow and the cathode flow channels are as follows: the inlet flow rates are constant, the inlet gas compositions are constant, and the flows are fully developed at the outlets of the anode and cathode flow channels. At the solid walls, non-slip and zero fluxes hold. At the interfaces between the gas channels, the diffuser layers, the catalyst layers, and the PEM, equality is applied to the velocity, mass fraction, momentum flux, and mass flux. In this study, all the above conservation equations and property equations are solved by utilizing a general purpose

computational fluid dynamic code, CFD-ACE+, employing a finite volume method, released by ESI-CFD Inc. [19], since it has the ability to handle this moving boundary problem. The "moving boundary problem" actually implies that the boundary of the gas channel is subject to change during each iteration of the process.

The coupled set of equations was solved iteratively, and the solution was considered to be convergent when the relative error in each field between two consecutive iterations was less than a specified small number.

3. Shape generation for gas channel

The reason for using a B-spline curve for optimal channel shape is that it can generalize a smooth curve that satisfies the desired current distribution and makes it a proper shape for a channel; therefore the coordinates of the control points become the parameters that need to be estimated in this shape design problem to determine the optimal gas channel geometry.

Let us consider a Cartesian product parametric B-spline curve [20] given by

$$\Psi(t) = \sum_{j=1}^{n+1} B_j N_{j,k}(t) \quad t_{\min} \le t \le t_{\max};\ 2 \le k \le n+1, \tag{26}$$

where B_j are the position vectors of the $n+1$ defining polygon vertices and $N_{j,k}(t)$ are the normalized B-spline basis functions. For the jth normalized B-spline basis function of order k (degree $k-1$), the basis functions $N_{j,k}(t)$ are defined by the Cox–deBoor recursion formulas. Specifically:

$$N_{j,1}(t) = \begin{cases} 1 & \text{if } x_j \le t \le x_{j+1} \\ 0 & \text{otherwise} \end{cases}$$

and

$$N_{j,k}(t) = \frac{(t - x_j)N_{j,k-1}(t)}{x_{j+k-1} - x_j} + \frac{(x_{j+k} - t)N_{j+1,k-1}(t)}{x_{j+k} - x_{j+1}}, \tag{27}$$

where the values of x_i are the elements of a uniform knot vector satisfying the relation $x_j \le t \le x_{j+1}$. The parameter t varies from $t_{\min}$ to $t_{\max}$ along the curve $\Psi(t)$, i.e., $\Psi(t)$ are the curve data points.

The N basis functions can be determined from the knot vector and the parameter value t. B_j are the required polygon net points (control points). If B_j are given, the curve data points $\Psi(t)$ can be calculated from Eq. (26).

4. The inverse design problem

The current density distributions in the outlet region of the gas channel are almost uniform in the channel's width direction, therefore the redesigned gas channel surface can be assumed as a two-dimensional surface, i.e., it varies only in the length (flow) and height directions, and the dimensions are all the same in the channel's width direction. This implies that we need to redesign the optimal shape of the gas channel only in the length–height cross-section, and this result is used to generate the redesigned gas channel surface in the width direction.

For the inverse geometry design problem, the shape of the redesigned portion of the gas channel is regarded as being unknown and controlled by a set of control points; in addition, the desired distributions of current density located on the upper CP surface of the redesigned gas channel at the cathode are considered available.

Let the desired current densities located on the upper CP surface of the redesigned gas channel at the cathode be denoted by $Y(x_i, y_i) \equiv Y_i$, $i = 1$ to M, where M represents the number of grid points for the redesigned portion of the gas channel. The inverse geometry design problem can then be stated as follows: utilizing the above

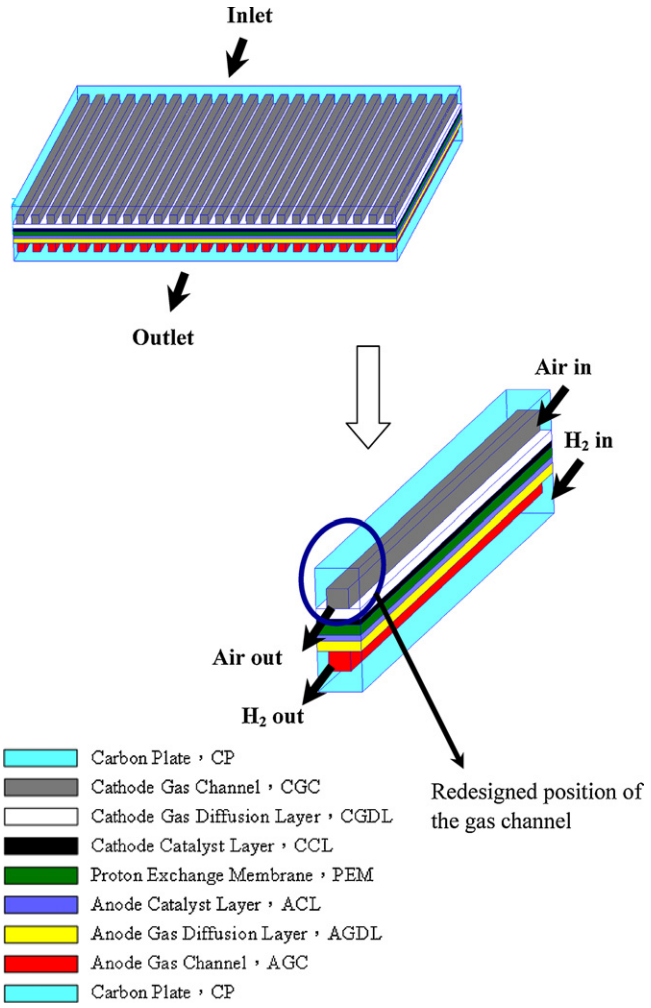

Fig. 1. Physical model of a single-cell, parallel straight channel PEMFC.

mentioned desired current densities Y_i, design the new shape for the gas channel.

The solution of the present inverse geometry design problem is to be obtained in such a way that the following functional is minimized:

$$J[\Psi(B_j)] = \sum_{i=1}^{M} [I_{c,i}(B_j) - Y_i]^2 = U^T U; \quad j = 1 \text{ to } P. \tag{28}$$

Here, $I_{c,i}$ represent the estimated or computed current densities at the channel locations (x_i, y_i). These quantities are determined from the solution of the direct problem given previously by using an estimated gas channel $\Psi(B_j)$, with P representing the number of control points.

4.1. The Levenberg–Marquardt method (LMM) for minimization

If the redesigned portion of the gas channel is discretized into M points and P control points are used, Eq. (28) is minimized with respect to the estimated parameters B_j to obtain:

$$\frac{\partial J[\Psi(B_j)]}{\partial B_j} = \sum_{i=1}^{M} \left[\frac{\partial I_{c,i}}{\partial B_j}\right] \left[I_{c,i} - Y_i\right] = 0; \quad j = 1 \text{ to } P, \tag{29}$$

where M should be equal to or greater than P, otherwise an underdetermined system of equations will be obtained, and it

Table 1
Fixed parameters used by CFD-ACE+ code in the present study.

Parameters	Symbols	Values
Reference transfer current density at anode **($A\,m^{-2}$)	$I_{a,ref}$	9E+008
Reference transfer current density at cathode ($A\,m^{-2}$)	$I_{c,ref}$	2.5E+002
Anodic charge transfer coefficients for anode reaction	$\alpha_{a,a}$	0.5
Cathodic charge transfer coefficients for anode reaction	$\alpha_{a,c}$	0.5
Anodic charge transfer coefficients for cathode reaction	$\alpha_{c,a}$	1.5
Cathodic charge transfer coefficients for cathode reaction	$\alpha_{c,c}$	1.5
Thickness of carbon plate (m)	d_{CP}	2E−003
Width of rib (m)	W_R	1E−003
Resistivity of carbon plate (ohm-m)	Ω_{CP}	2.7E−004
Length of gas channel (m)	L_{CH}	5E−002
Height of gas channel (m)	H_{CH}	1E−003
Width of gas channel (m)	W_{CH}	1E−003
Anode inlet gas velocity ($m\,s^{-1}$)	v_a	0.3
Cathode inlet gas velocity ($m\,s^{-1}$)	v_c	0.5
Anode inlet mass fraction of H_2	$Z_{H_2,a}$	0.445
Anode inlet mass fraction of H_2O	$Z_{H_2O,a}$	0.555
Cathode inlet mass fraction of O_2	$Z_{O_2,c}$	0.212
Cathode inlet mass fraction of N_2	$Z_{N_2,c}$	0.709
Cathode inlet mass fraction of H_2O	$Z_{H_2O,c}$	0.079
Thickness of gas diffusion layer (m)	d_{GDL}	0.3E−003
Porosity of gas diffusion layer (m^2)	ε_{GDL}	0.5
Permeability of gas diffusion layer (m^2)	k_{GDL}	1.76E−011
Bruggemann coefficient of gas diffusion layer	θ_{GDL}	1.5
Electronic conductivity of gas diffusion layer ($\Omega^{-1}\,m^{-1}$)	σ_{GDL}	300
Thickness of catalyst layer (m)	d_{CL}	1E−005
Porosity of catalyst layer (m^2)	ε_{CL}	0.112
Permeability of catalyst layer (m^2)	k_{CL}	1.76E−011
Bruggemann coefficient of catalyst layer	θ_{CL}	1.5
Electronic conductivity of catalyst layer ($\Omega^{-1}\,m^{-1}$)	σ_{CL}	300
Thickness of membrane (m)	d_m	5E−005
Porosity of membrane (m^2)	ε_m	0.28
Permeability of membrane (m^2)	k_m	5E−018
Bruggemann coefficient of membrane	θ_m	13

will be impossible to calculate the inverse solutions. Eq. (29) is linearized by expanding $I_{c,i}(B_j)$ in Taylor series and retaining the first-order terms. Then a damping parameter μ^n is added to the resulting expression to improve convergence, leading to the Levenberg–Marquardt method [21], given by

$$(\mathbf{F} + \mu^n \boldsymbol{\Xi})\Delta\mathbf{B} = \mathbf{D} \tag{30}$$

$$\mathbf{F} = \boldsymbol{\vartheta}^{\mathrm{T}}\boldsymbol{\vartheta} \tag{31}$$

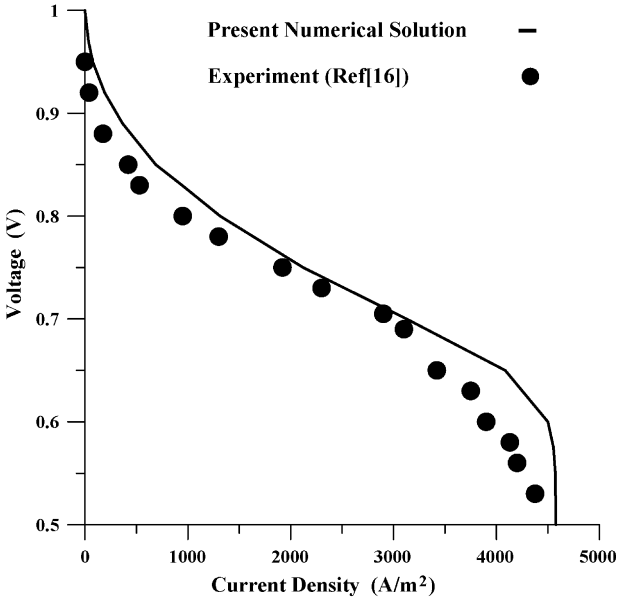

Fig. 2. Comparison of the numerical and experimental polarization curves.

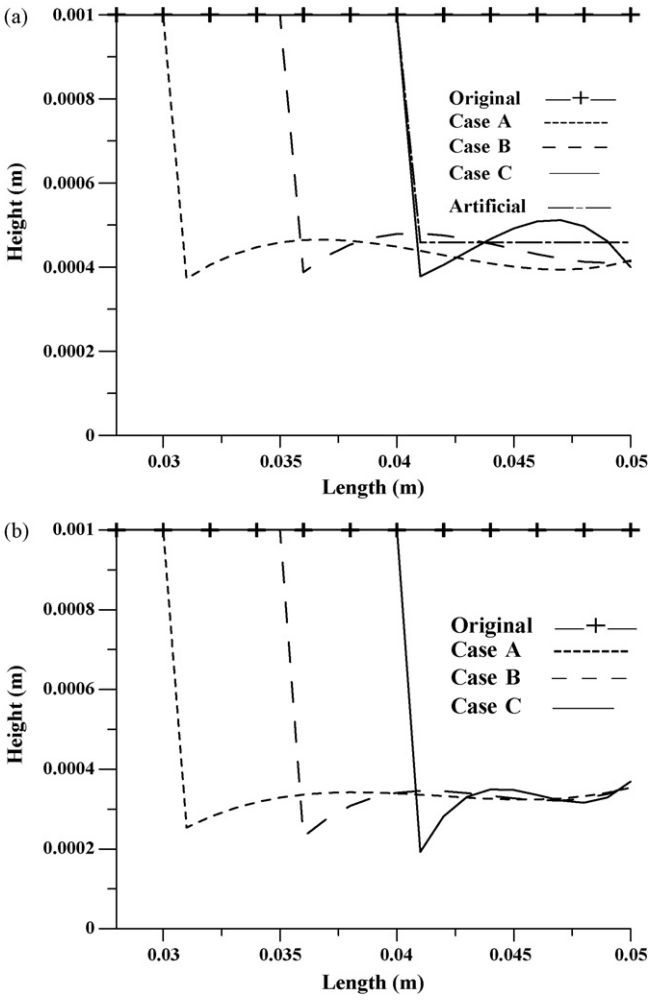

Fig. 3. The original and estimated optimal shapes of gas channels at (a) 0.4 V and (b) 0.7 V, with 20% increase in the local current density.

$$\mathbf{D} = \boldsymbol{\vartheta}^{\mathrm{T}}\mathbf{U} \tag{32}$$

$$\Delta\mathbf{B} = \mathbf{B}^{n+1} - \mathbf{B}^{n}. \tag{33}$$

Here, the superscripts n and T represent the iteration index and transpose matrix, respectively, $\boldsymbol{\Xi}$ is the identity matrix, and ϑ denotes the Jacobian matrix, defined as

$$\boldsymbol{\vartheta} = \frac{\partial \mathbf{I}_c}{\partial \mathbf{B}^{\mathrm{T}}}. \tag{34}$$

The Jacobian matrix defined by Eq. (34) is determined by perturbing the unknown parameters B_j one at a time and computing the resulting change in current density from the solution of the direct problem, Eqs. (1)–(25).

Eq. (30) is now written in a form suitable for iterative calculation as

$$\mathbf{B}^{n+1} = \mathbf{B}^{n} + (\boldsymbol{\vartheta}^{\mathrm{T}}\boldsymbol{\vartheta} + \mu^n \boldsymbol{\Xi})^{-1}\boldsymbol{\vartheta}^{\mathrm{T}}(\mathbf{I}_c - \mathbf{Y}). \tag{35}$$

When $\mu^n = 0$, Newton's method is obtained, and as $\mu^n \to \infty$, the steepest-descent method is obtained. For fast convergence the steepest-descent method is applied first, then the value of μ^n is decreased, and finally Newton's method is used to obtain the inverse solution. The algorithm for choosing this damping value μ^n is described in detail by Marquardt [21], so it is not repeated here.

The bridge between CFD-ACE+ and LMM is the INPUT/OUTPUT files. These files should be arranged such that their format can be

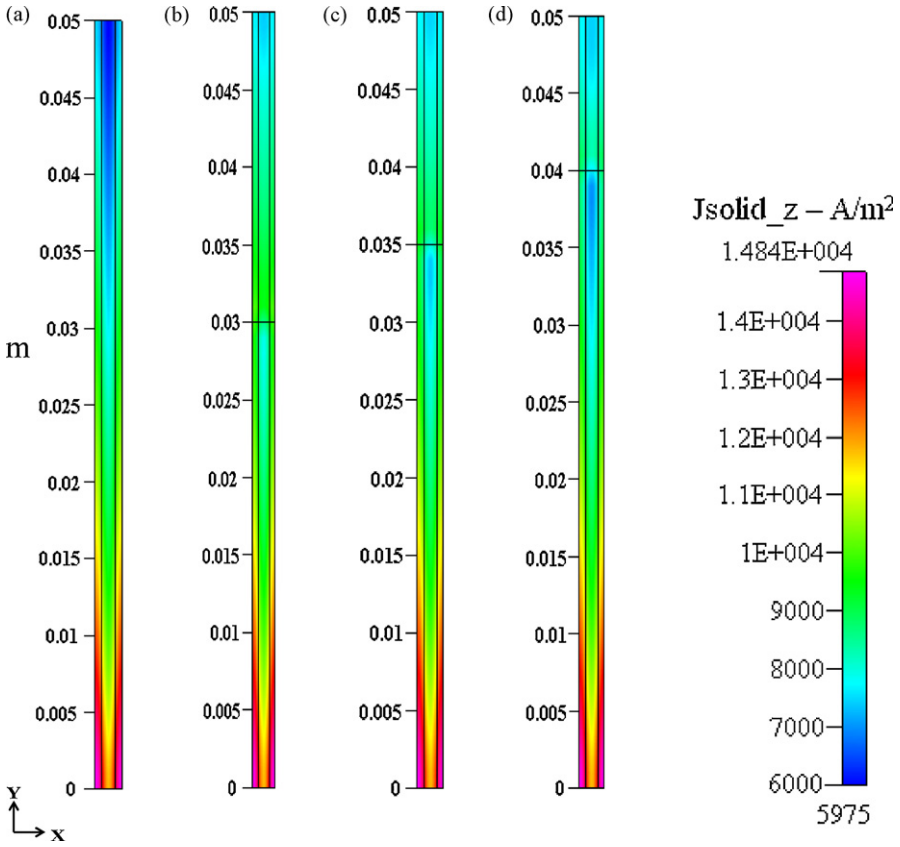

Fig. 4. The current density distributions for (a) original case, (b) Case A, (c) Case B and (d) Case C gas channels at 0.4 V, with 20% increase in the local current density.

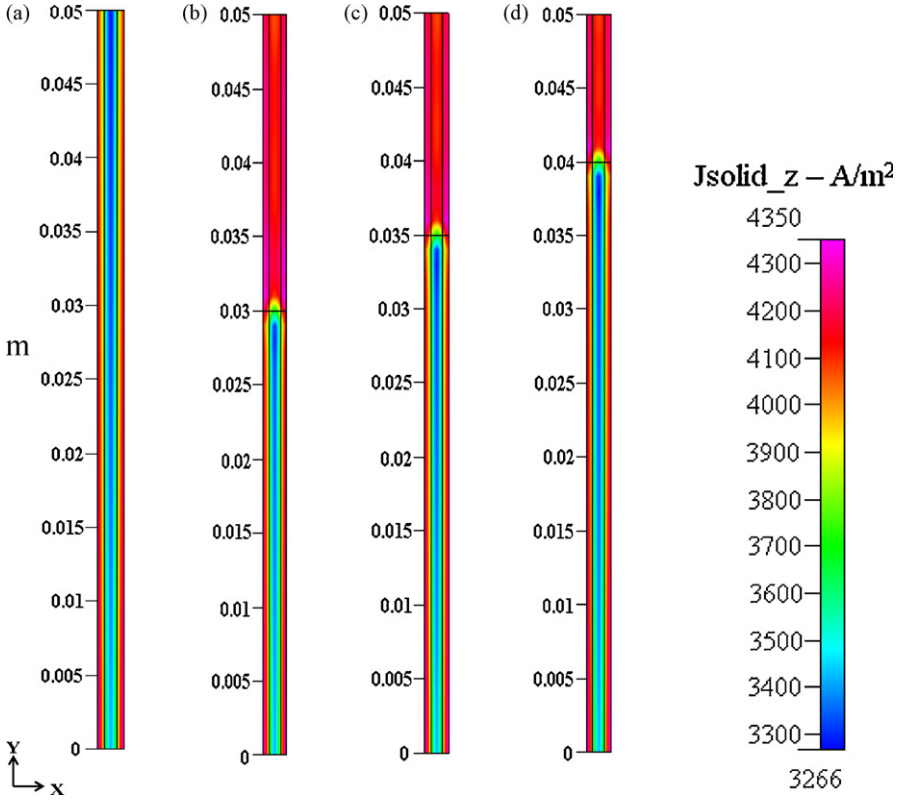

Fig. 5. The current density distributions for (a) original case, (b) Case A, (c) Case B and (d) Case C gas channels at 0.7 V, with 20% increase in the local current density.

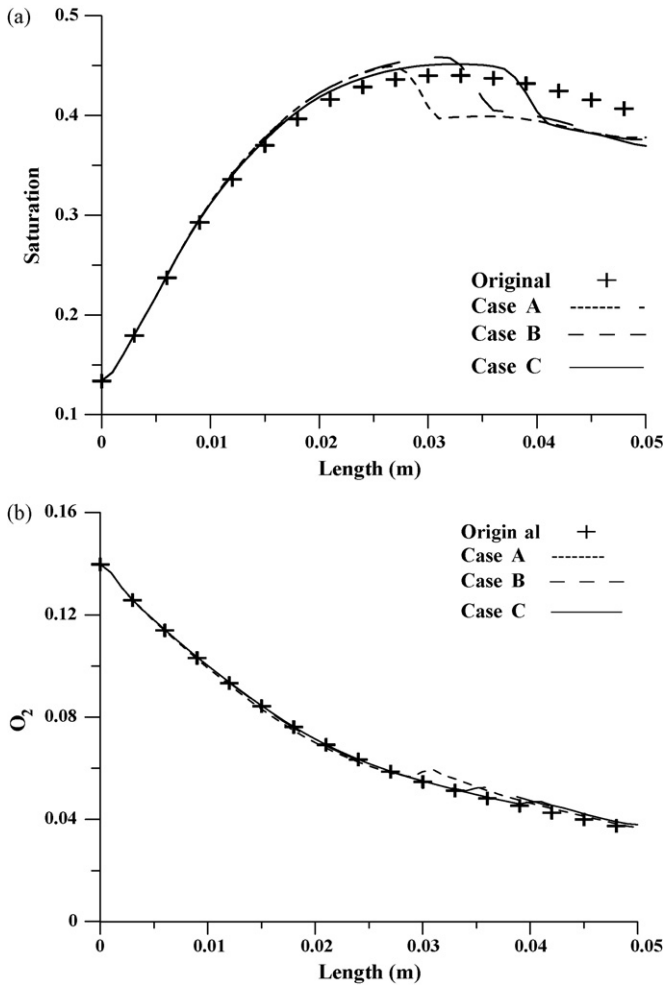

Fig. 6. The original and calculated (a) saturations and (b) oxygen concentrations along the center line of the cathode GDL–CL interface at 0.4 V, with 20% increase in the local current density.

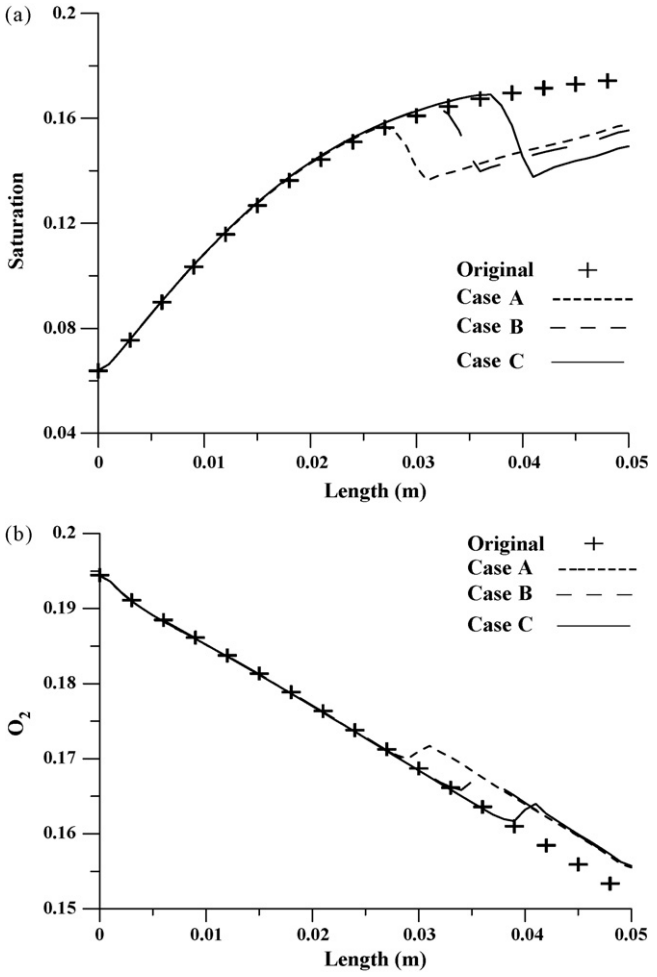

Fig. 7. The original and calculated (a) saturations and (b) oxygen concentrations along the center line of the cathode GDL–CL interface at 0.7 V, with 20% increase in the local current density.

recognized by CFD-ACE+ and LMM. A sequence of forward PEMFC problems is solved by CFD-ACE+ in an effort to update the gas channel geometry by minimizing a residual measuring the difference between estimated and desired current densities located on the upper CP surface of the redesigned gas channel at the cathode under the present algorithm.

5. Computational procedure

The iterative computational procedure for the solution of this inverse design problem using the Levenberg–Marquardt method can be summarized as follows:

Step 1. Choose the initial guess for control points **B** (obtained by using the original shape of the gas channel and B-spline curve fitting) at iteration n to start the computations.
Step 2. Solve the direct problem given by Eqs. (1)–(25) to obtain computed current densities $\mathbf{I}_c$.
Step 3. Construct the Jacobian matrix in accordance with Eq. (34).
Step 4. Update **B** from Eq. (35).
Step 5. Check the stopping criterion; if not satisfied go to Step 2 and iterate.

6. Results and discussion

The accuracy of the solution from CFD-ACE+ plays a very important role in this inverse design problem. If the solution from CFD-ACE+ cannot reproduce the actual performance of the PEMFC, the inverse solutions can never be obtained accurately. The first task is thus to show the validity of the solutions from CFD-ACE+ by comparing them with existing experimental data.

The benchmark problem for the numerical solution using CFD-ACE+ is examined here based on the experiments conducted by Cheng et al. [16]. The grid system for a single-cell fuel cell module with a cross-sectional area of 22 cm × 22 cm and an active area of 14 cm × 14 cm has been constructed. Two 2-mm thick composite graphite plates are used as the flow fields and current conductors. A five-layer membrane exchange assembly (MEA) is placed at the center between the two composite graphite plates. Fig. 1 shows the present single-cell PEMFC. For simplicity, only one gas channel is computed in the present study, as in Cheng et al. [16]. The inlet velocities for the hydrogen and the air are chosen as 0.3 and 0.5 m s^{-1}, respectively. The hydrogen and the air are humidified to reach 100% relative humidity and 80 °C temperature before entering the gas flow channels. The operating and geometrical conditions given to the direct problem solver are consistent with the experiments. The fuel cell temperature is maintained at 70 °C. The fixed

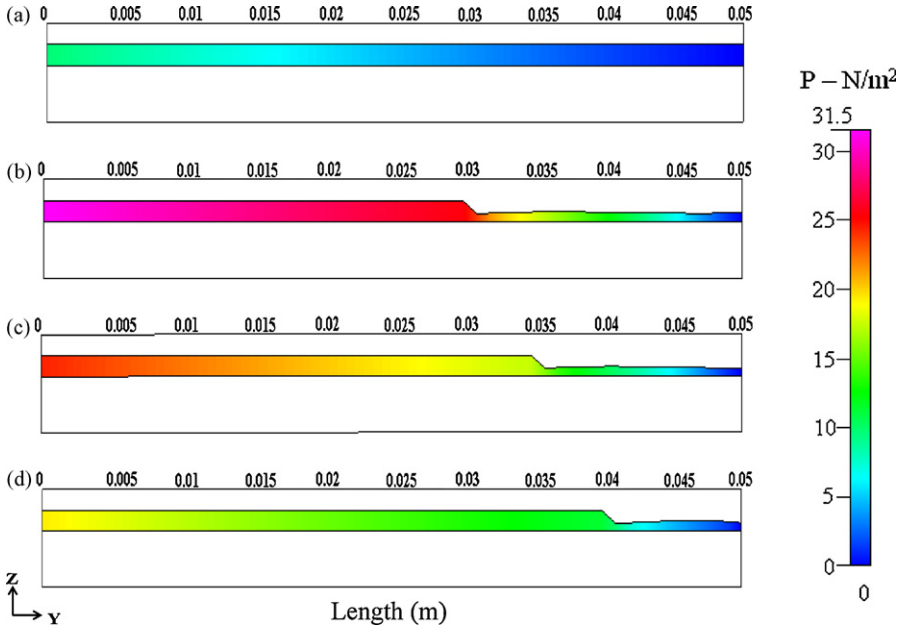

Fig. 8. The pressure distributions for (a) original case, (b) Case A, (c) Case B and (d) Case C gas channels at 0.4 V, with 20% increase in the local current density.

parameters used for the numerical calculations in CFD-ACE+ are listed in Table 1.

Fig. 2 illustrates the comparisons between the numerical solutions using CFD-ACE+ and the experimental data from [16] for the polarization curves. It is obvious that the numerical solutions from CFD-ACE+ match well with the experimental data. Three gas channel design problems will be considered here, differing by the starting point of the redesigned channel:

(1) Case A: the redesigned channel length equals 20 mm (from 30 to 50 mm),
(2) Case B: the redesigned channel length equals 15 mm (from 35 to 50 mm), and
(3) Case C: the redesigned channel length equals 10 mm (from 40 to 50 mm).

The number of control points is taken as four in all the examples considered here, and the design criterion is that the current density on the upper CP surface of the redesigned channel is required to increase by 20% of the original current density (for a rectangular gas channel) at 0.4 V (low operating voltage) and 0.7 V (high operating voltage). One should note that even though more control points describe the unknown surface more accurately, they also require more computer time to obtain the inverse solutions.

The inverse calculations are performed by using the Levenberg–Marquardt method based on the above conditions. The initial estimates of B_j are obtained via B-spline curve fitting for

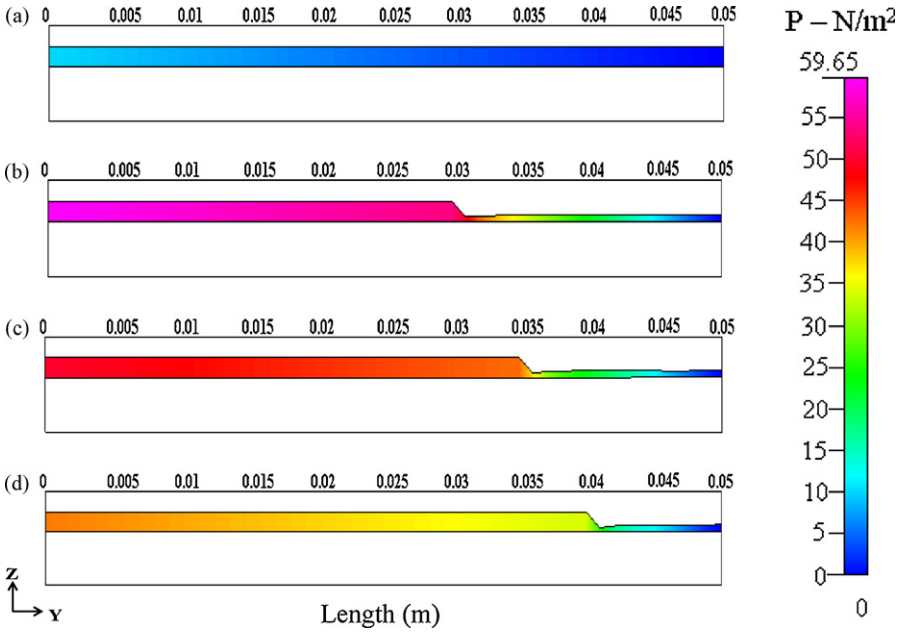

Fig. 9. The pressure distributions for (a) original case, (b) Case A, (c) Case B and (d) Case C gas channels at 0.7 V, with 20% increase in the local current density.

Table 2
Polarization data for the original and various redesigned channels with 20% increase in the local current density.

Voltage (V)	Original total current density ($A\,m^{-2}$)	Case A (0.4 V) total current density ($A\,m^{-2}$)	Case B (0.4 V) total current density ($A\,m^{-2}$)	Case C (0.4 V) total current density ($A\,m^{-2}$)	Case A (0.7 V) total current density ($A\,m^{-2}$)	Case B (0.7 V) total current density ($A\,m^{-2}$)	Case C (0.7 V) total current density ($A\,m^{-2}$)
0.97	285	328	372	359	369	411	387
0.95	404	455	437	423	505	479	453
0.92	563	619	599	583	673	645	616
0.89	786	847	826	808	906	876	844
0.85	1,158	1,227	1,203	1,184	1,293	1,258	1,224
0.83	1,384	1,456	1,431	1,411	1,525	1,489	1,452
0.80	1,785	1,863	1,836	1,814	1,935	1,897	1,858
0.75	2,653	2,739	2,710	2,686	2,818	2,776	2,734
0.70	3,776	3,872	3,840	3,813	3,958	3,912	3,866
0.65	5,095	5,208	5,169	5,139	5,298	5,248	5,198
0.60	6,495	6,637	6,588	6,551	6,735	6,677	6,620
0.58	7,172	7,338	7,282	7,241	7,444	7,379	7,317
0.55	7,782	7,987	7,925	7,873	8,104	8,032	7,961
0.50	8,677	8,961	8,876	8,804	9,121	9,019	8,920
0.40	9,482	9,848	9,723	9,638	10,029	9,895	9,777
0.30	9,729	10,102	9,981	9,879	10,303	10,156	10,006

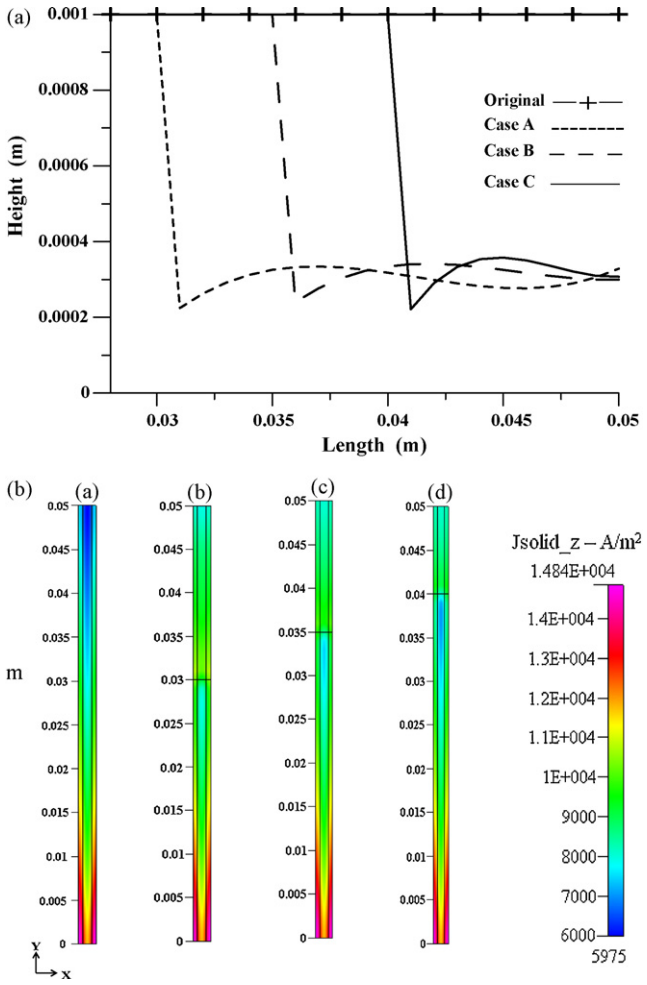

Fig. 10. The original and estimated (a) optimal shape of gas channels and (b) current density distributions at 0.4 V, with 30% increase in the local current density.

the rectangular gas channel. After only 7–10 iterations (the CPU time on an Intel Dual-core 1.8 GHz processor is about 3–4 days), the estimated shape of the gas channel can be obtained, and this result is shown in Fig. 3(a) and (b). The average relative errors for the desired and calculated current density on the upper surface of the redesigned channel are calculated as 2.5% (Case A at 0.4 V), 2.4% (Case B at 0.4 V), 2.5% (Case C at 0.4 V), 2.7% (Case A at 0.7 V), 2.7% (Case B at 0.7 V), and 2.6% (Case C at 0.7 V), where the average relative error ERR is defined as

$$\mathrm{ERR} = \sum_{i=1}^{M} \left| \frac{I_{c,i} - Y_i}{Y_i} \right| \times 100 \div M, \tag{36}$$

where M = 120, 90 and 60 for cases A, B and C, respectively. It is obvious from these errors that the Levenberg–Marquardt method has been applied successfully for estimating the optimal shape of gas channels in the numerical examples, since the calculated current densities closely agree with the desired ones. The overall increased percentages for the current in these six cases are obtained as 3.9% (Case A at 0.4 V), 2.5% (Case B at 0.4 V), 1.6% (Case C at 0.4 V), 4.8% (Case A at 0.7 V), 3.6% (Case B at 0.7 V), and 2.4% (Case C at 0.7 V), respectively.

Fig. 3(a) and (b) shows the original and redesigned optimal shapes for gas channels at operating voltages of 0.4 and 0.7 V, respectively. The redesigned optimal gas channels exhibit oscillatory profiles, and the first point of the redesigned channel is always

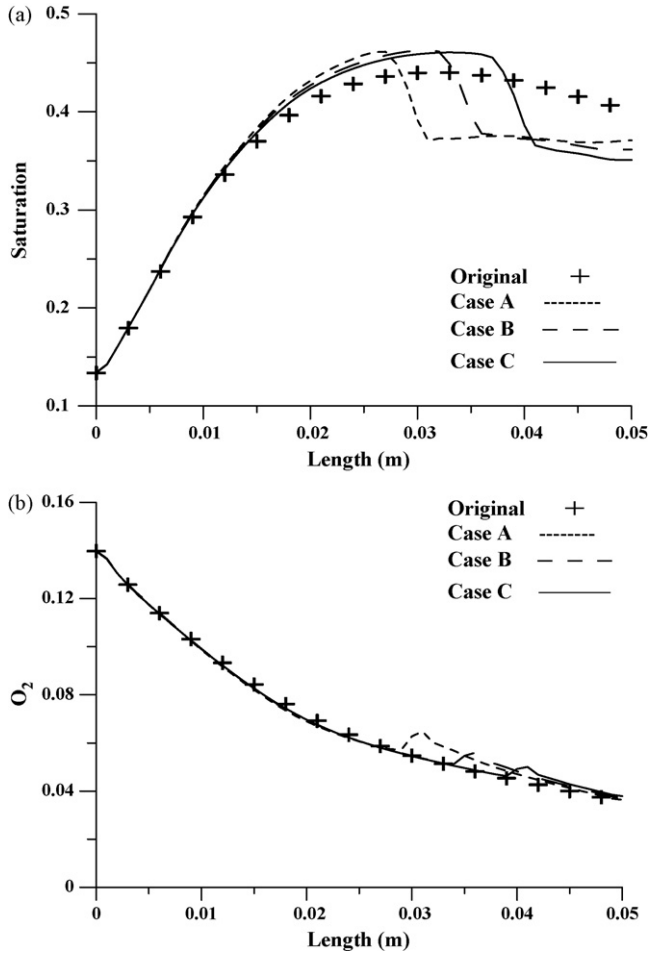

Fig. 11. The original and calculated (a) saturations and (b) oxygen concentrations along the center line of the cathode GDL–CL interface at 0.4 V, with 30% increase in the local current density.

at the lowest position. This may be due to the fact that at the first point, a sudden increase in the desired current density is required; to obey this requirement, a sudden contraction of the gas channel is needed. However, at the adjacent section of the channel, the height does not have to be corrected as low as that in the first position to match the desired current density; therefore, the profile of the gas channel increases in height smoothly, and then decreases in height smoothly if necessary.

To show that the estimated shape is indeed the optimal shape, we have considered an artificial rectangular gas channel with a sudden contraction and the same duct volume as Case C at 0.4 V. Fig. 3(a) shows the profile for this artificially contracted gas channel. The direct solution is then calculated based on this gas channel, and the average relative error for the desired and calculated current density on the upper surface of the redesigned channel is calculated as 2.7%, which is greater than that for the optimal gas channel. The overall increase in the current is 1.4%, which is also smaller than that for the optimal gas channel. It can therefore be concluded that the performance of the PEMFC with an optimal redesigned gas channel is indeed better than its performance with the artificial gas channel. Figs. 4 and 5 indicate the original and calculated current density on the cathode CP surface for Cases A, B and C at 0.4 and 0.7 V, respectively. It is obvious from these two figures that the current densities in the redesigned gas channels are all higher than those for the original gas channel.

From Fig. 3(a) and (b), we found that in order to match the desired current density, the gas channel must be contracted suddenly at the start of the redesigned position of the gas channel, in order to remove the saturated water as well as to increase the concentration of oxygen. The above statements can be verified by plotting the calculated water saturation and oxygen concentration with channel length. Here, water saturation is defined as the ration of the liquid water volume in the porous medium to the total volume of the porous medium. Fig. 6(a) and (b) indicate the original and calculated saturation and oxygen concentration along the center line of the gas channel and on the cathode GDL–CL interface, respectively, for Cases A, B and C, at the low operating voltage of 0.4 V, while Fig. 7(a) and (b) shows the same for the high operating voltage of 0.7 V.

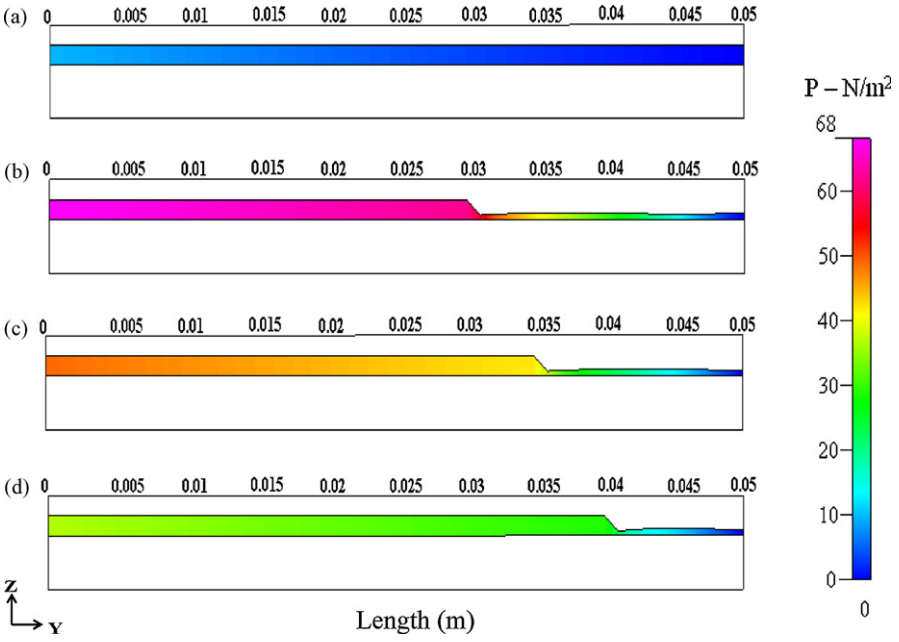

Fig. 12. The pressure distributions for (a) original case, (b) Case A, (c) Case B and (d) Case C gas channels at 0.4 V, with 30% increase in the local current density.

Table 3
Polarization data for the original and various redesigned channels with 30% increase in the local current density.

Voltage, V	Original total current density ($A\,m^{-2}$)	Case A (0.4 V) total current density ($A\,m^{-2}$)	Case B (0.4 V) total current density ($A\,m^{-2}$)	Case C (0.4 V) total current density ($A\,m^{-2}$)
0.97	285	456	416	386
0.95	404	526	484	452
0.92	562	696	650	615
0.89	785	932	882	843
0.85	1158	1,321	1,265	1,222
0.83	1383	1,555	1,496	1,451
0.8	1785	1,967	1,905	1,857
0.75	2653	2,853	2,785	2,732
0.7	3775	3,996	3,921	3,864
0.65	5094	5,341	5,258	5,196
0.6	6494	6,785	6,687	6,617
0.575	7171	7,499	7,393	7,313
0.55	7781	8,164	8,045	7,956
0.5	8677	9,190	9,032	8,909
0.4	9482	10,115	9,917	9,760
0.3	9729	10,381	10,156	10,005

From Figs. 6(a) and 7(a), we found that the longer the redesigned channel, the more saturated water will be removed, and that the saturation at 0.4 V is more than that at 0.7 V. Contrarily, the oxygen concentration at 0.4 V is less than that at 0.7 V. This is because the electrochemical reaction is more moderate at 0.7 V than at 0.4 V, and as a result less oxygen will be consumed and less water will be produced at 0.7 V. This also explains why the overall increase of current at 0.4 V is higher than that at 0.7 V. From Figs. 6(b) and 7(b), at the redesigned position of the original gas channel, the oxygen concentration for 0.4 V is much lower than that for 0.7 V. This implies a perfect reaction at 0.4 V. By imposing the requirement that the redesigned current density be 20% greater than the original current density at the redesigned position, the amount of the increment of oxygen concentration at 0.4 V is also almost consumed when compared with the case at 0.7 V, and therefore the overall increase of current at 0.4 V is greater than that at 0.7 V.

The pressure is also an important index for this design problem, since it will be increased for the optimal gas channel. Figs. 8 and 9 indicate the pressure distributions along the gas channel at 0.4 and 0.7 V, respectively, for the original case, Case A, Case B and Case C at 0.4 and 0.7 V. It is obvious that the longer the redesigned gas channel, the larger the pressure difference. If this pressure drop cannot be handled by the gas pumping system, the optimally designed gas channel cannot be used.

Table 2 shows the polarization data based on the optimal gas channels, Case A, Case B and Case C, designed for 0.4 and 0.7 V, when operating at any other voltages. It is obvious that these designs are for 0.4 and 0.7 V, but can still be applied to different operating voltages to ensure increase of the overall current.

The next question is whether the current density on the upper CP surface of the redesigned channel can be required to increase by 30% of the original current density (for a rectangular gas channel) at 0.4 V (low operating voltage) and 0.7 V (high operating voltage). The inverse calculations are performed again, using the Levenberg-Marquardt method based on the above conditions.

Unfortunately, at 0.7 V, the design fails, since it is impossible to obtain the needed shape to match the desired current density. However, at 0.4 V, it can be estimated successfully. Fig. 10(a) shows the original and estimated optimal shapes for gas channel at 0.4 V. The tendency of the designed optimal gas channels is similar to the previous estimations. The average relative errors for the desired and calculated current densities on the upper CP surface of the redesigned channel are calculated as 2.8% (Case A at 0.4 V), 2.6% (Case B at 0.4 V) and 2.7% (Case C at 0.4 V), and again the calculated current densities closely agree with the desired densities. The overall increased percentages for the current in the present cases are obtained as 6.7% (Case A at 0.4 V), 4.6% (Case B at 0.4 V) and 2.9% (Case C at 0.4 V).

Fig. 10(b) indicates the original and calculated current densities for Cases A, B and C at 0.4 V. Fig. 11(a) and (b) shows the original and calculated saturation and oxygen concentration along the center line of the gas channel and on the cathode GDL–CL interface for Cases A, B and C at 0.4 V. By comparing Fig. 11(a) with Fig. 7(a) and Fig. 11(b) with Fig. 7(b), it can be seen that more water is removed and higher oxygen concentration is obtained under this redesigned condition. Fig. 12 indicates the pressure distributions along the gas channel for the original case, Case A, Case B and Case C at 0.4 V. It is obvious by comparing Figs. 8 and 12 that the higher the desired current density, the larger the pressure difference.

Table 3 indicates the polarization data based on the optimal gas channels, Case A, Case B and Case C, designed at 0.4 V, when operating at any other voltages. Again, the design at 0.4 V can still be applied to different operating voltages to obtain better performance from the fuel cell. Based on the above numerical experiment, it is concluded that the design problem of determining the optimal shape for a PEMFC fuel cell gas channel using the Levenberg–Marquardt method is now completed. The calculated current density can match well with the desired value if the requirement is attainable.

7. Conclusions

An inverse design problem in estimating the optimal shape of gas channels for PEMFCs from the knowledge of desired current density distributions, using the techniques of B-spline curves and the Levenberg–Marquardt method, has been developed and applied successfully. Numerical experiments have been performed based on low and high operating voltages, in this case 0.4 and 0.7 V. The results reveal that the present algorithm needs only a few iterations to obtain the optimal shape of the gas channel, and the overall current can be increased by using the estimated gas channel.

The advantages of using the technique of the inverse design problem in designing the optimal shape of gas channels lie in the facts that (1) the time needed to redesign the channel can be shortened and (2) the desired current density can be well matched when compared with the traditional trial and error method.

Acknowledgment

This work was supported in part through the National Science Council, ROC, Grant number NSC-97-2221-E-006-262-MY3.

References

[1] W. Sun, B.A. Peppley, K. Karana, J. Power Sources 144 (2005) 42.
[2] E. Hontanon, M.J. Escudero, C. Bautista, P.L. Garcia-Ybarra, L. Daza, J. Power Sources 86 (2000) 363.
[3] T. Berning, N. Djilali, J. Power Sources 124 (2003) 440.
[4] C.Y. Wang, Chem. Rev. 104 (2004) 4727.
[5] M. Secanell, et al., Electrochim. Acta 52 (2007) 2668.
[6] H.H. Lin, C.H. Cheng, C.Y. Soong, F. Chen, W.M. Yan, J. Power Sources 162 (2006) 246.
[7] S.W. Cha, R. O'Hayre, S.J. Lee, Y. Saito, F.B. Prinz, J. Electrochem. Soc. 151 (2004) 1856.
[8] M.V. Williams, H.R. Kunz, J.M. Fenton, J. Electrochem. Soc. 151 (2004) A1617.
[9] W.M. Yan, C.Y. Soong, F.L. Chen, H.S. Chu, J. Power Sources 143 (2005) 48.
[10] F.B. Weng, A. Su, C.Y. Hsu, C.Y. Lee, J. Power Sources 157 (2006) 674.
[11] C. Xu, Y.L. He, T.S. Zhao, R. Chen, Q. Ye, J. Electrochem. Soc. 153 (2006) A1358.
[12] D.H. Ahmed, H.J. Sung, J. Power Sources 162 (2006) 327.
[13] C.H. Huang, C.C. Chiang, S.K. Chou, J. Ship Res. 42 (1998) 79.
[14] P.F. Chen, C.H. Huang, J. Ship Res. 46 (2002) 138.
[15] P.F. Chen, C.H. Huang, M.C. Fang, J.H. Chou, J. Ship Res. 50 (2006) 1.
[16] C.H. Cheng, H.H. Lin, G.J. Lai, J. Power Sources 165 (2007) 803.
[17] W.M. Yan, H.C. Liu, C.Y. Soong, F.L. Chen, C.H. Cheng, J. Power Sources 161 (2006) 907.
[18] T.E. Springer, T.A. Zawodzinski, S. Gottesfeld, J. Electrochem. Soc. 138 (1991) 2334.
[19] CFD-RC User's Manual, ESI-CFD Inc., 2005.
[20] D.F. Rogers, J.A. Adams, Mathematical Elements for Computer Graphics, 2nd edition, McGraw-Hill, 1990.
[21] D.M. Marquardt, J. Soc. Ind. Appl. Math. 11 (1963) 431.